

First Fast Radio Burst Search Campaign at the Argentine Institute of Radio Astronomy

Downloaded from: https://research.chalmers.se, 2026-11-27 07:44 UTC

Citation for the original published paper (version of record):
Lousto, C., Prajapati, H., Zubieta, E. et al (2026). First Fast Radio Burst Search Campaign at the Argentine Institute of Radio Astronomy. Astrophysical Journal, 1012(1).
http://dx.doi.org/10.3847/1538-4357/aeb6b9

N.B. When citing this work, cite the original published paper.

research.chalmers.se offers the possibility of retrieving research publications produced at Chalmers University of Technology. It covers all kind of research output: articles, dissertations, conference papers, reports etc. since 2004. research.chalmers.se is administrated and maintained by Chalmers Library

(article starts on next page)

The Astrophysical Journal, 1012:70 (12pp), 2026 November 20 https://doi.org/10.3847/1538-4357/aeb6b9
© 2026. The Author(s). Published by the American Astronomical Society.
OPEN ACCESS

First Fast Radio Burst Search Campaign at the Argentine Institute of Radio Astronomy

Carlos O. Lousto[1], Harsh Prajapati[2], Ezequiel Zubieta[3], Susana B. Araujo Furlan[4,5], Guillermo Gancio[3], Joaquín Pelle[6], Gustavo E. Romero[3], Federico García[3], Santiago del Palacio[3,7], and Nathan Cahill[8]
[1] Center for Computational Relativity and Gravitation, Rochester Institute of Technology, Rochester, NY 14623, USA; colsma@rit.edu
[2] Center for Imaging Science, Rochester Institute of Technology, Rochester, NY 14623, USA
[3] Instituto Argentino de Radioastronomía (CCT La Plata, CONICET; CICPBA; UNLP), C.C.5, (1894) Villa Elisa, Buenos Aires, Argentina
[4] Facultad de Matemática, Astronomía, Física y Computación, UNC, Av. Medina Allende s/n, Ciudad Universitaria, X5000HUA Córdoba, Argentina
[5] Instituto de Astronomía Teórica y Experimental, CONICET-UNC, Laprida 854, X5000BGR Córdoba, Argentina
[6] Max Planck Institute for Gravitational Physics (Albert Einstein Institute), Am Mühlenberg 1, 14476 Potsdam, Germany
[7] Department of Space, Earth and Environment, Chalmers University of Technology, SE-412 96 Gothenburg, Sweden
[8] School of Mathematics and Statistics, Rochester Institute of Technology, Rochester, NY 14623, USA
Received 2026 August 10; revised 2026 October 16; accepted 2026 October 17; published 2026 November 13

Abstract

Fast radio bursts (FRBs) are intense millisecond-duration radio transients of extragalactic origin whose physical nature remains under investigation, and which also probe the intergalactic medium. We report on the first FRB search campaign carried out at the Argentine Institute of Radio Astronomy (IAR), between 2024 December and 2026 March, targeting nearby galaxy superclusters in the southern sky. We observed fields in the Ophiuchus, Shapley, and Sculptor/Phoenix supercluster regions with one of the two 30 m antennas of the IAR, using a ROACH-based backend with 400 MHz of bandwidth centered at 1400 MHz and a time resolution of 41–82 μs, for a total net observing time of 212 hr. The data were searched for dispersed single pulses with `PRESTO` in the dispersion measure (DM) range of $100 \leqslant \mathrm{DM} \leqslant 500\,\mathrm{pc\,cm^{-3}}$, and candidates were classified with the `FETCH` machine learning classifier, validated on archival Parkes data containing known FRBs and on synthetic bursts injected into IAR observations. One FRB candidate, FRB 20251018, was identified on 2025 October 18 in an observation pointed toward the galaxy cluster A2870, in the Phoenix supercluster, with a DM of $243 \pm 20\,\mathrm{pc\,cm^{-3}}$, a signal-to-noise ratio of 8.2, and a `FETCH` score of $p = 0.99$. To the best of our knowledge, it would, if confirmed, be the first FRB detected from South America. A set of more marginal candidates is also presented. These results demonstrate the capability of the IAR antennas to detect FRBs and support extending the monitoring campaign to coincident dual-antenna observations and crossmatches with gravitational-wave events and electromagnetic transients.

Unified Astronomy Thesaurus concepts: Radio transient sources (2008); Radio astronomy (1338); Extragalactic radio sources (508); Radio bursts (1339)

1. Introduction

Fast radio bursts (FRBs) are intense millisecond-duration radio pulses of extragalactic origin. The first was found in 2007 in archival Parkes data (D. R. Lorimer et al. 2007), with a dispersion measure (DM) of $\sim$375 pc cm^{-3} far in excess of any plausible Galactic contribution. Its astrophysical nature was debated for several years, in part because of the terrestrial *perytons* that mimicked it (E. Petroff et al. 2015), until the detection of four further bursts at high Galactic latitude with DMs up to 1100 pc cm^{-3} established FRBs as a genuine cosmic population (D. Thornton et al. 2013). Thousands of events have since been detected (M. Amiri et al. 2021), most with DMs of 200–1200 pc cm^{-3} and inferred distances from $\sim$100 Mpc to a few Gpc, at an all-sky rate of order $10^4\,\mathrm{sky^{-1}\,day^{-1}}$ above a fluence of $\sim$3 Jy ms at 1.4 GHz (D. Thornton et al. 2013), corresponding to a volumetric rate of $\sim 10^7\,\mathrm{Gpc^{-3}\,yr^{-1}}$ for luminosities above 10^{38} erg s^{-1} (V. Ravi 2019; W. Lu et al. 2020). Bursts have been detected from $\sim$100 MHz (Z. Pleunis et al. 2021a) to 8 GHz (V. Gajjar et al. 2018), with durations from tens of microseconds to tens of milliseconds, single or multicomponent morphologies, and typical fluences of 1–100 Jy ms (D. J. Champion et al. 2016; K. W. Bannister et al. 2017; W. Farah et al. 2018; J. W. T. Hessels et al. 2019; C.-H. Niu et al. 2021; D. J. Zhou et al. 2022). Their isotropic distribution on the sky is consistent with an extragalactic origin (S. Bhandari et al. 2018).

A fraction of FRBs repeat, with waiting times from milliseconds to weeks (L. G. Spitler et al. 2016; CHIME/FRB Collaboration 2020). The repeater FRB 121102 enabled the first host galaxy identification, at $z \sim 0.19$ (S. Chatterjee et al. 2017), and the growing sample of localized bursts has established the correlation between extragalactic DM and redshift known as the Macquart relation (J.-P. Macquart et al. 2020). The apparently nonrepeating population is likely a mixture of genuinely one-off events and sources that repeat too rarely to have been caught, and the morphological differences reported between the two classes should be read as population tendencies rather than rules: repeaters tend to show broader, more complex bursts with narrower spectra, whereas one-off bursts tend to be simpler and narrower (M. Amiri et al. 2021; Z. Pleunis et al. 2021b). The only FRB with an identified progenitor is the Galactic burst from the magnetar SGR 1935+2154, detected in coincidence with an X-ray burst (C. D. Bochenek et al. 2020; S. Mereghetti et al. 2020); its energy of $\sim 10^{35}$ erg is far below that of extragalactic FRBs, but its morphology is similar, supporting magnetars as the engine of at least part of the population (B. D. Metzger et al. 2019; Y. Lyubarsky 2020; B. Zhang 2023). The combination of

Original content from this work may be used under the terms of the Creative Commons Attribution 4.0 licence. Any further distribution of this work must maintain attribution to the author(s) and the title of the work, journal citation and DOI.

millisecond durations, cosmological distances, and brightness temperatures above 10^{35} K requires coherent emission from compact, highly magnetized regions (J. I. Katz 2016). Beyond the question of their origin, FRBs have become probes of the intergalactic medium: the DM–z relation accounts for the "missing baryons" (M. McQuinn 2013; J.-P. Macquart et al. 2020), and larger samples promise constraints on dark energy, reionization and large-scale structure (Z.-X. Li et al. 2018; A. Walters et al. 2018; P. Beniamini et al. 2021; M. Rafiei-Ravandi et al. 2021; M. Shirasaki et al. 2022).

The Argentine Institute of Radio Astronomy (IAR), located at a latitude of $-34°51'57\farcs35$ and longitude $-58°08'25\farcs04$, operates two 30 m single-dish antennas, aligned along the north–south direction and separated by 120 m. They cover a decl. range of $-90° < \delta < -10°$ and an h.a. range of 2 hr east/west, $-2\ \mathrm{hr} < t < 2\ \mathrm{hr}$. Observations are conducted using both radio telescopes, named after Carlos M. Varsavsky and Esteban Bajaja (hereafter A1 and A2), in dual polarization (with both circular components combined) centered at 1400 MHz (L band). In G. Gancio et al. (2020), we provided a thorough description of the initial Ettus configuration of the front ends of A1 and A2, together with an analysis of the radio frequency interference (RFI) environment showing that the 1–2 GHz band has a low level of RFI activity, adequate for radio astronomy, even though the IAR is not located in an RFI-quiet zone. In mid-2022, we added a parallel digitizer system based on Reconfigurable Open Architecture Computing Hardware (ROACH) boards (J. Hickish et al. 2016). The ROACH-1 backends,[9,10] installed on both A1 and A2, observe in dual circular polarization over a bandwidth of 400 MHz with integration times down to 41 or 82 μs, and provide a theoretical improvement by a factor of up to $\sim$2.5 in the signal-to-noise ratio (S/N) with respect to the Ettus boards with 56 MHz of bandwidth, a rounded figure that follows from the $\sqrt{\Delta\nu}$ scaling of the radiometer sensitivity to a broadband pulse ($\sqrt{400/56} \simeq 2.7$; see Equation (7) of C. O. Lousto et al. 2024), the exact gain depending on the fraction of each band lost to interference in a given observation. Our observational schedule focuses on high-cadence observations, reaching daily cadence for some pulsars (E. Zubieta et al. 2025a, 2025b, 2024, 2023; C. O. Lousto et al. 2026) and magnetars (S. B. Araujo Furlan et al. 2026), with individual observations as long as 3.66 hr day^{-1}. A short review of the observing capabilities of the IAR after the upgrade, and of the science programs they enable, is given in C. O. Lousto et al. (2024).

Two features of the IAR make a modest single-dish FRB program worthwhile despite its limited sensitivity. First, its longitude gives it observing windows with little overlap with those of other high-cadence facilities: southern sources are visible from the IAR at times when they are largely inaccessible from Europe, Asia, Australia, and South Africa, as we quantified for the magnetar XTE J1810−197 (S. B. Araujo Furlan et al. 2026), so that its monitoring adds temporal coverage rather than duplicating deeper surveys. Second, its flexible scheduling permits daily cadence on a chosen field for months, which is what a search for repetition requires. We therefore target nearby galaxy superclusters, whose 30′ fields contain many galaxies within a few tens of Mpc, so that a burst from a member galaxy would arrive with a modest DM and a relatively high fluence—the regime that a 30 m antenna can reach—while background bursts seen through the same fields extend the reach to $z \lesssim 0.2$. The DM search range follows from this target selection and is discussed in Section 2.

In this work, we use the data from the A2 ROACH receiver to present the first blind FRB search campaign carried out at the IAR, covering observations taken between 2024 December and 2026 March. Section 2 describes the search pipeline, Section 3 the observations, Section 4 the validation tests and the candidates, and Section 5 discusses the results and the prospects of the program.

2. Search Pipeline

With thousands of hours of good-quality pulsar observations, it is interesting to investigate whether the data also contain FRB signals (E. Petroff et al. 2019). In particular, machine learning techniques have been developed to perform massive searches for FRBs (Y. G. Zhang et al. 2018) and to classify them (K. L. Wagstaff et al. 2016; L. Connor & J. van Leeuwen 2018), using both supervised (J.-W. Luo et al. 2022) and unsupervised methods (B. H. Chen et al. 2021; J.-M. Zhu-Ge et al. 2022). A practical implementation for fast transient classification (D. Agarwal et al. 2020) is `FETCH`.[11] Another useful tool is the synthetic FRB generator `FRB-faker`[12] (L. J. M. Houben 2020; L. J. M. Houben et al. 2026), which can be used to train FRB search and classification algorithms. A living theoretical catalog of FRBs, with a review of the numerous existing theories proposed to model them, is presented in E. Platts et al. (2019); see also the list of theoretical scenarios at https://frbtheorycat.org/index.php/Main_Page and the list of observed FRBs at https://www.frbcat.org. Another FRB catalog is reported in J. Xu et al. (2023).

The Petabyte Project maintains a comprehensive list of FRB software,[13] which includes data read and write packages (`your`), single-pulse search (`PRESTO`), single-pulse injection (`FRB-faker`), machine learning classifiers (`FETCH`), population synthesis of FRBs, catalogs and tools for catalogs, burst analysis software, visualizations, RFI mitigation (`RFI-Clean`), and containers. The codes given in parentheses are those with which we have hands-on experience. New FRB findings can also be cross-checked for coincidences with gravitational-wave detections, as recently attempted in R. Abbott et al. (2023).

Our single-pulse search pipeline proceeds as follows. RFI is first excised in two stages: `RFIClean` (Y. Maan et al. 2021) removes periodic interference in the Fourier domain, and `rfifind` (`PRESTO`, run with `-time 1 -freqsig 4 -intfrac 0.3 -chanfrac 0.4 -zerodm`) then produces a time–frequency mask, to which the channel lists of Section 3 are added with `-zapchan`. The dedispersion plan is generated with `DDplan.py`, and the filterbank data are dedispersed with `prepsubband` (`PRESTO`; S. Ransom 2011), using 32 subbands over a grid of trial DMs covering the chosen search range of $100 \leqslant \mathrm{DM} \leqslant 500\ \mathrm{pc\ cm^{-3}}$ in steps of 1 pc cm^{-3}, with the output time series downsampled by a factor of 8 (to 0.33

[9] https://casper.astro.berkeley.edu/wiki/ROACH
[10] https://digicom.org/roach-board.html
[11] https://github.com/devanshkv/fetch
[12] https://gitlab.com/houben.ljm/frb-faker
[13] https://github.com/thepetabyteproject/frbsoft

and 0.66 ms for the observations sampled at 40.96 and 81.92 μs, respectively). The resulting time series are searched with `single_pulse_search.py` with a detection threshold of 8σ and boxcar widths of up to 45 samples (`max_downfact`), i.e., up to $\simeq$29 ms at the downsampled resolution. The surviving candidates are converted into HDF5 cutouts with `your_candmaker.py` (from the `your` package; K. Aggarwal et al. 2020) and classified with the FETCH deep-learning classifier (model A), retaining candidates with $p > 0.5$ for visual inspection, where p is the score assigned by the network to a candidate being a genuine astrophysical burst rather than RFI (D. Agarwal et al. 2020). This last step provides the bulk of the data reduction: a typical observation yields several thousand single-pulse triggers above the 8σ threshold—the overwhelming majority of them low-level RFI—of which FETCH retains of order half a dozen with $p > 0.5$, a number small enough for every surviving candidate to be inspected individually by eye. The FETCH score is a classifier output trained on other telescopes' data, not a calibrated probability of astrophysical origin for IAR interference; we therefore use $p > 0.5$ only as a preselection, and no candidate is retained on the basis of its FETCH score alone (Section 4). The behavior of the classifier on the interference of the site can nevertheless be measured directly, and it differs between the two populations of triggers we encounter. A search of the FRB 20251018 observation over $0 \leqslant \mathrm{DM} \leqslant 100\,\mathrm{pc\,cm^{-3}}$, a range dominated by narrow impulsive terrestrial signals, produced 71,160 triggers above 8σ, almost all of them a few samples wide; FETCH did not assign $p \geqslant 0.5$ to any of them, an upper limit of 4×10^{-5} (95% confidence) on its false-positive rate for that population. In the survey range, by contrast, the triggers are dominated by wide-boxcar responses to low-frequency baseline fluctuations, and FETCH retains of order half a dozen of the several thousand time-grouped events above 8σ in a typical observation, i.e., $\sim 2 \times 10^{-3}$; it is this second population, to which FRB 20251018 belongs by its boxcar width, that the visual inspection is designed to filter. On genuine pulses, FETCH retains 80% of Vela's single pulses above 8σ and 67% of those with $\mathrm{S/N} = 8$–10 (Section 4.1).

The DM search range was set by the expected DM budget of the targeted superclusters rather than by the FRB population at large. Toward the four fields the NE2001 (J. M. Cordes & T. J. W. Lazio 2002) and YMW16 (J. M. Yao et al. 2017) models give Galactic disk contributions of 228 and 142 $\mathrm{pc\,cm^{-3}}$ (Ophiuchus, $b = 10.5°$), 59 and 45 (Shapley, $b = 32.3°$), 31 and 12 (A4013, $b = -71.2°$), and 31 and 20 (A2870, $b = 70.0°$), to which a Galactic halo term of $\sim$30–50 $\mathrm{pc\,cm^{-3}}$ at high latitude (S. Yamasaki & T. Totani 2020) and a cosmic term of $\simeq$20–50 $\mathrm{pc\,cm^{-3}}$ for $z \simeq 0.02$–0.05 (J.-P. Macquart et al. 2020) must be added. A burst from a member galaxy of the three high-latitude superclusters is therefore expected at a total DM $\simeq$ 60–250 $\mathrm{pc\,cm^{-3}}$, depending on its host contribution, and one from the Ophiuchus field at $\simeq$200–500 $\mathrm{pc\,cm^{-3}}$; background sources seen through the fields extend the range upward. The adopted lower bound of 100 $\mathrm{pc\,cm^{-3}}$ excludes the low-DM local interference that dominates the trigger population, and most Galactic pulsars and rotating radio transients toward the high-latitude fields (though not toward Ophiuchus, where Galactic sources with DM up to $\sim$230 $\mathrm{pc\,cm^{-3}}$ are possible). It also excludes, however, member-galaxy bursts with host contributions below $\sim$40–70 $\mathrm{pc\,cm^{-3}}$, and the upper bound of 500 $\mathrm{pc\,cm^{-3}}$ truncates the Ophiuchus budget and excludes background bursts with substantial host or intracluster contributions. The rate limits of Section 4.4 therefore apply to the searched DM range only. Extending the search to $\simeq$30–1000 $\mathrm{pc\,cm^{-3}}$ with an adaptive dedispersion plan—coarser DM steps and heavier downsampling at high DM, which would limit the additional cost—is deferred to a future processing of the data; the present results should be read with the incompleteness described above.

The validation of this pipeline, on archival Parkes data containing seven known FRBs, on synthetic bursts injected into IAR observations, and on single pulses from bright pulsars observed with the same antenna and backend, is presented in Section 4.1, with further details in Appendix B.

3. Observations at IAR

There are essentially two strategies one can follow to observe FRBs with the IAR antennas. The first is to observe regions of the sky that are expected to produce FRBs, such as nearby galaxy clusters. The second is to track known FRBs in order to look for repeaters. Given an all-sky rate of order 10^4 FRBs $\mathrm{sky^{-1}\,day^{-1}}$ above $\sim$3 Jy ms (D. Thornton et al. 2013; E. Petroff et al. 2019), the detection rate for a beam of solid angle $\Delta\Omega \approx \pi\theta^2_{\mathrm{FWHM}}/4$ is $\dot{N}_{\mathrm{IAR}} \sim \dot{N}_{\mathrm{FRB}}\,\Delta\Omega/4\pi$, i.e., one burst per $\sim$500 hr if every burst above 3 Jy ms were detectable. Our fluence threshold is an order of magnitude higher (Section 4.4), and for a Euclidean fluence distribution ($N(>\mathcal{F}) \propto \mathcal{F}^{-3/2}$) the accessible rate is lower by a factor of $\sim$25, so that a detection would be expected only after $\sim 10^4$ hr. The campaign reported here was conceived as a pilot to establish the capability and the candidate-selection procedure rather than to reach that exposure.

The biggest challenge in the search for FRBs is that we do not know when or where the next one will occur. The radio sky must therefore be observed continuously until one of these events is captured. Since thousands of FRBs are thought to occur per day, serendipitous detections are feasible. This implies that large amounts of raw radio-astronomical data must be accumulated and analyzed. Observations with a bandwidth of 400 MHz, sampled every 82 μs in 512 frequency channels of 0.78 MHz, generate a typical data volume of 85 GB $\mathrm{hr^{-1}}$ of observation, corresponding to up to 2 TB $\mathrm{day^{-1}}$ and 0.75 PB $\mathrm{yr^{-1}}$. Given that the IAR observatory can track sources for up to 3.66 hr $\mathrm{day^{-1}}$, any single observation may potentially contain an FRB signal, motivating the application of machine learning algorithms to search for such patterns in the accumulated raw data. As an illustration of the potential of such archival searches, S.-B. Zhang et al. (2019) reported the discovery of a new FRB (FRB 010312) in the original archival dataset of the first detection (FRB 010724), almost two decades later.

In our search for FRBs in the southern sky with A2, which has a primary beam of 30′ (FWHM), we avoid the Galactic center (R.A. $17^{\mathrm{h}}45^{\mathrm{m}}40\overset{\mathrm{s}}{.}05$, decl. $-29°00'28\overset{''}{.}1$) and the Galactic plane, focusing instead on nearby superclusters in the southern hemisphere that are also accessible within the observatory schedule. All coordinates quoted in this paper are in the J2000 epoch.

All fields were observed with the same standard configuration of the A2 ROACH backend: dual circular polarization (summed), with a bandwidth of 400 MHz divided into 512 channels of 0.78125 MHz, spanning 1200.8–1600.0 MHz

Table 1
Observational Summary for the Four Supercluster Fields (J2000 Pointing Centers)

Field	Pointing (R.A., Decl.)	Date (yyyy-mm)	Obs. (No.)	Total (s)	Total (hr)
Ophiuchus	$17^h10^m00^s$, $-22°00'00''$	2024-12	2	5896.28	1.6378
		2025-01	3	8798.17	2.4439
		Total	5	14,694.45	4.0817
Shapley	$13^h25^m00^s$, $-30°00'00''$	2024-12	10	53,418.03	14.8383
		2025-01	2	9981.42	2.7726
		Total	12	63,399.45	17.6109
Sculptor (A4013)	$23^h31^m54^s$, $-35°16'00''$	2025-04	3	17,865.19	4.9625
		2025-05	2	10,262.32	2.8506
		2025-07	2	19,323.01	5.3675
		2025-08	7	45,731.58	12.7032
		2025-09	6	42,826.84	11.8963
		2025-10	11	80,028.13	22.2300
		2026-01	5	19,016.32	5.2823
		2026-02	7	27,432.12	7.6200
		2026-03	10	36,520.24	10.1445
		Total	53	29,9005.74	83.0571
Phoenix (A2870)	$01^h07^m42^s$ $-46°55'00''$	2025-04	8	39,391.66	10.9421
		2025-05	9	56,144.47	15.5956
		2025-06	9	38,092.31	10.5811
		2025-07	14	45,234.42	12.5651
		2025-08	10	58,225.58	16.1737
		2025-09	6	42,758.98	11.8774
		2025-10	10	62,156.69	17.2657
		2026-01	2	13,485.02	3.7458
		2026-02	3	16,531.78	4.5921
		2026-03	2	14,274.41	3.9651
		Total	73	386,295.31	107.3041
Campaign total			143	763,394.95	212.0538

Note. All fields were observed with the A2 ROACH backend; the grand total is 143 observations and 212.05 hr.

(centered at 1400.4 MHz), and recorded as 32-bit SIGPROC filterbank files. The Ophiuchus and Shapley fields, observed between 2024 December and 2025 January, were sampled at 40.96 μs, whereas the longer Sculptor and Phoenix campaigns were carried out at 81.92 μs to halve the data volume; both sampling times vastly oversample the expected millisecond burst widths, given that the intra-channel dispersion smearing at a DM $\simeq 250\,\mathrm{pc\,cm^{-3}}$ already amounts to $\sim$0.6 ms at the center of the band. Individual pointings typically lasted between $\sim$0.8 and $\sim$2 hr (e.g., 2920 and 4632 s for representative Ophiuchus and Shapley observations, and $\sim$7110–7130 s for the A4013 and A2870 fields), within the maximum tracking time of 3.66 hr.

Ophiuchus supercluster—(R.A. $17^h10^m00^s$, decl. $-22°00'00''$). The Ophiuchus supercluster is a nearby galaxy supercluster in the constellation Ophiuchus, which forms the far wall of the Ophiuchus Void. It is centered on the cD cluster (Abell class type I) Ophiuchus Cluster and includes at least two additional galaxy clusters, four galaxy groups, and several field galaxies. Our observations focus on the central region of the supercluster. Notably, the Ophiuchus Cluster hosts a sharply truncated cool core (N. Werner et al. 2016) and a giant cavity, $\sim$0.5 Mpc across, filled with low-frequency radio emission that has been interpreted as the fossil of one of the most energetic active galactic nucleus outbursts known, powered by the supermassive black hole of the central galaxy (S. Giacintucci et al. 2020). A summary of the observations analyzed is given in Table 1.

Shapley supercluster—(R.A. $13^h25^m00^s$, decl. $-30°00'00''$). Identified as a single, exceptionally massive concentration of clusters in 1989 (S. Raychaudhury 1989; R. Scaramella et al. 1989), it is named after Harlow Shapley, who first noted an excess of galaxies in this region of the sky in the 1930s. The Shapley supercluster is a massive structure that has been the subject of numerous studies; although it is not the largest known supercluster, it is certainly one of the densest. It contains at least twenty rich galaxy clusters, among thousands of galaxy groups, including three of the richest galaxy clusters known: A3558, A3559, and A3560. We focus on a fairly central location near A3556 and A1736 in order to include several of these galaxy clusters within the primary beam of the radio telescope. A summary of the observations analyzed is given in Table 1.′

Sculptor region—(multiple pointings; Sculptor Galaxy: R. A. $23^h13^m14^s.02$, decl. $-28°21'26''.94$). Two superclusters in the Sculptor and Phoenix regions of the sky mark the position of a very long wall composed of thousands of galaxy groups stretching over nearly 300 Mpc, probably the longest of the nearby galaxy walls. The Sculptor superclusters are particularly important because they lie within this major wall of galaxies. We focus on a central region around the rich Abell cluster A4013 (R.A. $23^h31.9^m$, decl. $-35°16'$, $z \simeq 0.049$, i.e.,

Table 2
Channel-zapping Test of FRB 20251018

Stage	Mask	Live Band (MHz)	Range (MHz)	S/N	DM (pc cm^{-3})
1	`rfifind` flags only	≈360	1201–1600 (gaps)	8.26	243
2	channels 0, 15:18, 23:27, 63:71, 94:97, 115:122, 127, 135:140, 143:144, 220:234, 287, 362:365, 382:385, 428:438, 441:444, 476:490, 511	326	1202–1600	>8[a]	243
3	channels 0:30, 63:71, 75:146, 220:234, 287, 362:365, 382:385, 428:438, 441:444, 476:490, 511	270	1225–1600	>8[a]	243
4	static survey mask (Section 3)	264	1225–1600	>8[a]	243
5	channels 0:146, 159:175, 220:234, 272:274, 308:310, 362:365, 382:385, 410:511	170	1316–1521	8.20	243

Notes. Channel numbers follow the `PRESTO` convention (channel 0 at 1200.78 MHz). Stage 1 uses only the channels flagged by `rfifind` (run with `-time 1 -freqsig 4 -intfrac 0.3 -chanfrac 0.4 -zerodm`) (∼50 channels flagged for most of the observation, another ∼30 intermittently; the retained bandwidth is read from the mask plot and is approximate). Stages 2–5 add forced channel zapping (`-zapchan`) of increasing extent. Stage 5 is the mask of the cutout shown in Figure 1 and the bandwidth adopted for the flux density estimate. Stages 3 and 4 differ by only eight channels (5.5 MHz). The S/N of stage 1 is that of the discovery trigger, and the S/N of stage 5 is that of the cutout of Figure 1.
[a] Recovered above the 8σ threshold at DM = 243 pc cm^{-3}; the S/N values of these runs were not retained.

$d \approx 210$ Mpc for $H_0 = 70$ km s^{-1} Mpc^{-1}; G. O. Abell et al. 1989; M. F. Struble & H. J. Rood 1999; C. A. Valotto et al. 2004). A summary of the observations analyzed is given in Table 1.

The nearer of the two superclusters lies mainly within the constellation Phoenix and is therefore perhaps better referred to as the Phoenix supercluster. The six clusters in the Phoenix supercluster are all of richness class zero, meaning that none of them is particularly prominent. Our observations focus on a region centered around A2870 (R.A. $01^{h}07.7^{m}$, decl. $-46°55'$, $z = 0.0225$, i.e., $d \approx 96$ Mpc; G. O. Abell et al. 1989; M. F. Struble & H. J. Rood 1999). A summary of the observations analyzed is given in Table 1.

In processing these observations with `rfifind`/`PRESTO`, we applied an aggressive mask to filter out any potential source of local interference, thus reducing the effective bandwidth from the original 400 MHz to a net 264 MHz. Specifically, of the 512 channels into which the 400 MHz bandwidth is divided, we zapped channels 0:30, 63:71, 75:146, 170:175, 220:234, 273, 362:365, 382:385, 428:438, 441:444, 464, 476:490, and 511. The masked spectrum thus amounts to 135.94 MHz, and the clean (untouched) spectrum to 264.06 MHz. The single largest contiguous block of clean spectrum lies between channels 274 and 361, spanning 68.75 MHz of bandwidth. This static mask is applied identically to all four fields and is supplemented by the per-observation flagging produced by `rfifind`. Channel numbers follow the `PRESTO` convention, with channel 0 at the low-frequency edge (1200.78 MHz), so that the static mask retains 1225–1600 MHz. For the candidate in Section 4.2, we adopt, in addition, the most conservative of the masks used in the channel-zapping test (Table 2), which retains ≃170 MHz between 1316 and 1521 MHz, for the flux density estimate. Although this aggressive masking sacrifices ∼34% of the nominal bandwidth—and hence ∼19% in radiometer sensitivity—the interference is confined to stable, well-identified frequency ranges, so that the remaining 264 MHz of clean spectrum still exceeds the bandwidth of many successful single-dish FRB programs; we therefore do not regard the RFI environment as a fundamental limitation for future campaigns at the IAR, although the mask will be reevaluated periodically as the local spectrum occupancy evolves.

4. Results

4.1. Pipeline Validation

Before turning to the survey data, we verified, in four ways, that the observing and processing chain recovers dispersed millisecond pulses at their correct arrival times and DMs. The details of each test are given in Appendix B.

First, we ran the pipeline of Section 2 on the archival Parkes dataset of E. F. Keane & E. Petroff (2015), which contains seven published FRBs (FRB 010125, 010621, 010724, 110220, 110626, 110703, and 120127). All seven were recovered with the correct arrival times and DMs, and, in the same data, `PRESTO` produced fewer false positives than the `Heimdall` search (B. R. Barsdell et al. 2012; B. R. Barsdell & A. Jameson 2024) run in parallel, which is why `PRESTO` was adopted for the survey.

Second, we injected six synthetic bursts with `FRB-faker` into IAR filterbank data: one blind injection into the archival Parkes file containing FRB 110703 (DM = 1306 pc cm^{-3}, FWHM 3.4 ms, S/N = 14.5), recovered independently by three members of the team together with the real burst, and five bursts of common two-component morphology but different DM, arrival time, and S/N ($10 \leqslant S/N \leqslant 45$, $120 \leqslant DM \leqslant 560$ pc cm^{-3}; Table B1) injected into five 300 s zenith observations of A2 taken on 2024-09-23. All were recovered, at the `PRESTO` S/N between 8.3 and 29 and at DMs within -32 to $+8.5$ pc cm^{-3} of the injected values (Table B1); two of them, recovered at S/Ns = 8.3 and 9.5, probe the pipeline in the threshold regime of the survey.

Third, the same antenna and processing tools have been used for single-pulse work on known sources. A single-pulse search of XTE J1810−197 with `PRESTO`'s `single_pulse_search.py`, at the same 8σ threshold, over the same 100–500 pc cm^{-3} trial range in steps of 1 pc cm^{-3}, and with boxcar widths of 0.29–4.4 ms, recovered 249 giant pulses from the magnetar at its known DM = 178.8 ± 0.1 pc cm^{-3} with the A2 antenna (S. B. Araujo Furlan et al. 2026), albeit with the 56 MHz Ettus backend rather than the ROACH one; and with the ROACH backend itself, individual pulses of PSR J0835−4510 (Vela), PSR J1644−4559 and PSR J0437−4715 have been extracted at the pulsars' known DMs from A2 observations (C. O. Lousto et al. 2026), $\sim 1.5 \times 10^5$ per observation for Vela. Together, these establish that the observing chain—antenna, receiver, digitizer, RFI excision

and dedispersion—recovers millisecond pulses from the sky, not only injected ones. Neither test, however, passed the pulses through the FETCH stage of the FRB pipeline.

Fourth, we ran the survey pipeline itself on a 3549 s ROACH observation of PSR J0835−4510 (Vela) with antenna A2, with the `rfifind` mask alone and no forced channel zapping (stage 1 of Table 2), at the native 163.84 μs sampling of that observation, over a trial-DM range bracketing the pulsar's DM. Grouping the 2.72×10^6 triggers coincident in time leaves 38,683 events, of which 36,552 (94.5%) have their best DM within 5 pc cm^{-3} of the catalog value: these are the pulsar's own pulses, recovered in 92.1% of the 39,692 rotations in the segment, so that the 8σ threshold corresponds to about the 8th percentile of Vela's single-pulse brightness with this system. Their DMs have a mean of 67.80 and a scatter of 0.75 pc cm^{-3} (catalog value 68.0), their S/N a median of 14.3 (10th–90th percentiles 9.7–22.6), and their best-matching boxcars a median width of 1.5 ms (90th percentile 2.3 ms), matching the pulsar's cataloged $W_{50} = 1.7$ ms and 20 times narrower than the 29 ms boxcars that dominate the interference triggers of the survey (Section 2). The remaining 2131 events (5.5%), spread over the rest of the DM range and half of them at the widest boxcar, are the interference population of the observation. Finally, a random sample of 2000 of the pulsar events and 500 of the others was passed through `your_candmaker.py` and FETCH exactly as in the survey: 1603 of the 2000 pulses (80%) were classified with $p \geqslant 0.5$ (median $p = 0.98$), the fraction rising from 67% for S/N = 8–10 to 86% for S/N = 15–20, while eight of the 500 others (1.6%) passed. `FETCH` thus retains about two-thirds of genuine pulses at the survey threshold and four-fifths overall, and rejects ≃98% of the interference of this observation; the survey's completeness carries this factor in addition to the fluence limit of Section 4.4.

4.2. FRB 20251018

In the observations of the cluster A2870 (decl. $\delta = -46°55'00''$, R.A. $\alpha = 01^h07^m42^s$), we identified a candidate that has been preliminarily reported in an Astronomer's Telegram by our group as FRB 20251018 (H. Prajapati et al. 2026). To the best of our knowledge, it would, if confirmed, be the first FRB detected from South America. The decl. of −46°.55 quoted in the Telegram is a typographical error for −46°55′; the pointing center given here, which is that recorded in the observation headers, supersedes it.

This candidate appears in the observation of 2025 October 18, starting at MJD 60966.207662037035, at $t = 905.7474970$ s after the start of the observation (i.e., at MJD 60966.21814523), with a DM of DM = 243 ± 20 pc cm^{-3}, an observed width of $W \approx 6$ ms (FWHM), with the burst envelope spanning ≈25 ms at the base of the dedispersed profile shown in Figure 1, an S/N = 8.20 as reported by the search, and a FETCH score of $p = 0.99$. The width of ≈2.4 ms quoted in the discovery Telegram was read by eye from the candidate plot, whose time bins are 2.62 ms, and corresponds to the single-bin spike at the peak of the profile; the value of $W \approx 6$ ms adopted here is the FWHM measured on the same profile, and the matched boxcar returned by the search was 45 samples (29.5 ms), the widest available. The FWHM supersedes the Telegram value. Three widths are associated with the burst and must be kept apart. The FWHM of the dedispersed profile is ≈6 ms, and its boxcar-equivalent width, $W_{\rm eq} = \mathcal{F}/S_{\rm peak}$, is ≈9 ms. The boxcar at which

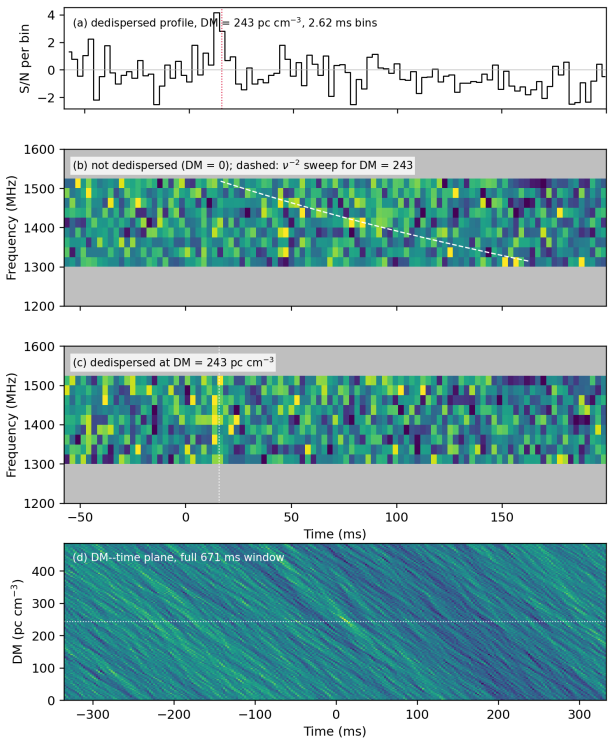

Figure 1. FRB candidate FRB 20251018 at MJD 60966.21814523 in the direction of the cluster A2870 (Phoenix supercluster), from the HDF5 cutout of the search pipeline (671 ms window, time resolution 2.62 ms). (a) Frequency-summed profile dedispersed at DM = 243 pc cm^{-3}, in units of the off-pulse rms; the dotted line marks the peak. (b) Dynamic spectrum *before* dedispersion, binned to 16 sub-bands of 25 MHz; the dashed curve is the ν^{-2} delay expected for DM = 243 pc cm^{-3}, anchored at the peak of the profile. (c) The same after dedispersion at DM = 243 pc cm^{-3}. In (b) and (c), gray marks sub-bands with no unmasked channels; the 217 live channels span 1316–1521 MHz (170 MHz), and sub-bands are normalized by their own off-pulse rms. Panels (a)–(c) show −60 to +200 ms around the nominal arrival time; (d) shows the DM–time (bowtie) plane over the full window, with the dotted line at DM = 243 pc cm^{-3}. The presentation follows that of X. Yang et al. (2021) for low-S/N candidates.

the search reported the trigger, 45 samples or 29.5 ms, is the widest searched, and it reflects the low-frequency baseline fluctuations of the time series rather than the burst: with the baseline removed by a running median, the matched boxcar S/N of the dedispersed time series is 5.2–6.3 for boxcars of 4–9 ms and falls to 4.6–5.4 at 29.5 ms, whereas without baseline removal it rises monotonically to 7.0 at 29.5 ms. The search value of 8.2, obtained with `PRESTO`'s block detrending at the widest boxcar, is therefore the detection statistic of the pipeline, but it is not the S/N of the burst at its own width, for which we adopt an S/N ≃ 6 (range 5.2–6.3). The burst, judged at its own width, thus lies below the nominal 8σ threshold and was recovered through the wide-boxcar response (Section 4.4). The candidate was identified with `PRESTO` and validated by the FETCH machine learning classifier; based on the radiometer equation—assuming a system temperature $T_{\rm sys} = 50 \pm 8$ K and an antenna gain $G \simeq 0.077$ K Jy^{-1} for A2 (corresponding to an aperture efficiency of ≃0.3), i.e., a system equivalent flux density SEFD ≃ 650 Jy (G. Gancio et al. 2020; S. B. Araujo Furlan et al. 2026)—with an S/N ≃ 6, $W_{\rm eq} \approx 9$ ms and the ≃170 MHz retained by the most conservative mask of the channel-zapping test described below, we estimate a band-averaged peak flux density of ≈2.2 ± 0.5 Jy and a fluence of

$\mathcal{F} \approx 20 \pm 5$ Jy ms, the uncertainties combining those of $T_{\rm sys}$ and of the S/N. The value of 3.9 ± 0.9 Jy quoted in the discovery report (H. Prajapati et al. 2026) used the search S/N of 8.2 with the FWHM of the profile and is superseded by the value given here. The quoted uncertainty on the DM is not the 1 pc cm^{-3} step of the search grid, which oversamples the time resolution, but the width of the S/N versus trial-DM response: for a burst of this width and S/N, detected over ≃170 MHz, the response peaks at DM ≃ 240 pc cm^{-3} and is consistent with the adopted value over a range of ≃±20 pc cm^{-3}, an uncertainty confirmed by the recovery of injected bursts of similar S/N and bandwidth (Appendix B).

Figure 1 shows the candidate at the resolution of the search cutout. At the S/N of this event, the dispersed sweep is not visible to the eye in the undedispersed dynamic spectrum (panel b): with an S/N ≃ 5 integrated over the 170 MHz of live bandwidth at 2.6 ms resolution, each of the nine live 25 MHz sub-bands carries only ≃1.7σ, and the same is true, for the same reason, of the vertical alignment in the dedispersed spectrum (panel (c)). The evidence that the signal is dispersed rests instead on the DM–time plane (panel (d)), in which the response is localized around DM ≃ 240 pc cm^{-3} and declines toward both lower and higher trial DMs, and on the channel-zapping test of Table 2.

To test whether the signal is confined to a narrow band of the spectrum, as is the case for most interference at the site, we reran the search on the same observation with progressively more aggressive channel masks, from the flags produced by `rfifind` alone down to the cleanest 170 MHz of the central band (Table 2). Persistence of the signal at a consistent DM as the bandwidth is reduced argues against narrowband interference. It does not by itself exclude broadband terrestrial signals, which are of two kinds. Undispersed impulses would have their maximum response at DM = 0: a dedicated search of the same observation over $0 \leqslant$ DM $\leqslant 100$ pc cm^{-3}, with the same pipeline and threshold, produced no trigger at the time of the candidate, and the trigger response of the event declines from an S/N ≃ 8.3 near DM = 240 to ≃5.7 at the lower edge of the survey range, which together exclude an undispersed origin at the sensitivity of the search. Swept-frequency signals are a different matter. The Parkes perytons (E. Petroff et al. 2015), traced to microwave ovens opened while running, mimic dispersion at apparent DMs of several hundred parsecs per cubic centimeter, and a low-DM search does not test for them; nor can a single-beam system apply the multibeam coincidence that identified the Parkes events. What we can say is limited. The Parkes perytons clustered in working hours and disappeared when the ovens were not in use, whereas no such equipment operates at the IAR and the candidate was recorded at 05:14 UTC (02:14 local time); their frequency sweeps departed from the cold-plasma ν^{-2} law, whereas the response of the candidate in the DM–time plane is consistent with it at the resolution available; and their durations of tens of milliseconds resemble the 29.5 ms trigger boxcar, though not the 6 ms profile width. Beyond this, we have no independent evidence against a swept-frequency terrestrial origin, a limitation intrinsic to single-dish, single-beam searches and a further reason for the candidate status. Coincident observations with the two IAR antennas would guard only against emitters local to one receiver; an independent detection remains the decisive test.

4.3. Marginal Candidates

Five additional, more marginal candidates—with lower FETCH scores and/or diagnostic plots of lower quality than those of FRB 20251018, but surviving our visual inspection against RFI contamination—are listed in Table A1 in Appendix A, where the downselection criteria are described. We list them for completeness and as a reference for crossmatching with independent detections at other wavelengths or facilities; we make no claim of astrophysical origin for any of them, and note in particular that the A4013 event of 2025 October 10, although it has both a higher S/N (9.23) and a higher FETCH score (0.997) than FRB 20251018, was judged less convincing on visual inspection: its dedispersed dynamic spectrum shows a bright narrowband feature at ≃1285 MHz that brightens at the candidate time, and its dedispersed profile has two peaks of comparable height rather than a single dominant pulse (Figure A1), both indicative of interference.

4.4. Rates and Upper Limits

For the system parameters of Section 4.2, the 8σ threshold corresponds to a minimum detectable fluence of $\mathcal{F}_{\rm min} \approx 7\,(W\ {\rm ms}^{-1})^{1/2}$ Jy ms for the nominal 264 MHz of clean bandwidth, and $\approx 9\,(W\ {\rm ms}^{-1})^{1/2}$ Jy ms for the 170 MHz retained by the most conservative mask (Appendix B); for bursts of width 6–9 ms the survey is thus complete to $\mathcal{F} \simeq$ 20–27 Jy ms; FRB 20251018, with $\mathcal{F} \approx 20$ Jy ms, lies at the edge of that range, consistent with its having been recovered at the widest boxcar rather than at its own width (Section 4.2). The exposure of the campaign is 212 hr × $\Delta\Omega/4\pi = 4.2 \times 10^{-5}$ sky days for the 30′ beam ($\Delta\Omega/4\pi \simeq 4.8 \times 10^{-6}$), so that one candidate corresponds to an all-sky rate of $\sim 2 \times 10^4$ sky^{-1} day^{-1} above ∼25 Jy ms, with a 95% confidence interval of 6×10^2–1.3×10^5 for a single Poisson event.

This must be compared with the FRB rate at the same fluence, not with the rates above ∼2–3 Jy ms measured by more sensitive telescopes. The most direct comparison is with ASKAP, whose fly's-eye survey found 37^{+26}_{-17} sky^{-1} day^{-1} above 26 Jy ms at 1.3 GHz (R. M. Shannon et al. 2018); scaling the Parkes rates of 10^4 above 3 Jy ms (D. Thornton et al. 2013) and 1.7×10^3 above 2 Jy ms (S. Bhandari et al. 2018) to 26 Jy ms with a Euclidean fluence distribution ($N(>\mathcal{F}) \propto \mathcal{F}^{-3/2}$) gives ∼400 and ∼40 sky^{-1} day^{-1}, respectively. The expected number of FRBs above our threshold in the 212 hr of the campaign is therefore $\sim 2 \times 10^{-3}$ to 2×10^{-2}, and one such event has a Poisson probability of only 0.2%–2% if FRB 20251018 is drawn from the known population. The implied rate is inconsistent with the ASKAP value even at its 95% lower bound. We see three readings of this tension, not mutually exclusive. The first is that the event is a rare, fortunate detection. The second is the premise of the survey itself: the fields were chosen because they contain nearby concentrations of hundreds of galaxies within the beam, and if a substantial fraction of FRBs at high fluence originate in the local volume traced by such structures, the rate toward them can exceed the all-sky average of wide-field surveys by a large factor. Whether it does is exactly what a targeted campaign of this kind can eventually measure, but one event cannot establish it. The third is that the event is not an extragalactic FRB. We regard the tension as a further reason to present FRB 20251018 as a candidate whose confirmation

requires either a repeat burst or an independent detection, and not as a reason to discard it.

For the fields without detections, the 95% Poisson upper limit of 3.0 events gives burst rates of $<0.73\,\mathrm{hr}^{-1}$ toward Ophiuchus (4.1 hr), $<0.17\,\mathrm{hr}^{-1}$ toward Shapley (17.6 hr) and $<0.036\,\mathrm{hr}^{-1}$ toward A4013 (83.1 hr), corresponding to all-sky rates of $<3.7\times10^{6}$, $<8.6\times10^{5}$, and $<1.8\times10^{5}\,\mathrm{sky}^{-1}\,\mathrm{day}^{-1}$ above $\sim$25 Jy ms; these limits apply to the searched DM range of 100–500 pc cm^{-3}, do not include the $\simeq$0.7–0.8 classifier completeness measured in Section 4.1 (which would raise both the limits and the implied rate by $\simeq$25%–50%), and are, as expected for such short exposures, far above the known FRB rate. The Ophiuchus limit in particular is weakened further by the fact that the Galactic disk contributes $\simeq$140–230 pc cm^{-3} along that sight line, so that member-galaxy bursts with a substantial host contribution would fall above the searched range.°

5. Discussion and Conclusions

The expected Milky Way contribution to the DM along the A2870 sight line ($l = 294.8°$, $b = -70.0°$) is small: the NE2001 (J. M. Cordes & T. J. W. Lazio 2002) and YMW16 (J. M. Yao et al. 2017) Galactic electron density models predict $\mathrm{DM_{MW}} \simeq 31$ and 20 pc cm^{-3}, respectively, to which an additional Galactic halo contribution of $\sim$30–50 pc cm^{-3} may be added (S. Yamasaki & T. Totani 2020). The resulting extragalactic excess at the nominal DM, $\mathrm{DM_{exc}} = \mathrm{DM_{obs}} - \mathrm{DM_{MW}} \simeq$ 170–220 pc cm^{-3} (150–240 once the uncertainty on the DM is included), sets—via the Macquart relation (J.-P. Macquart et al. 2020)—a conservative redshift upper limit of $z \lesssim 0.2$ if the host contribution is negligible. This comfortably encompasses the targeted cluster A2870 at $z = 0.0225$, for which the mean cosmic contribution is only $\sim$20 pc cm^{-3}; an origin in A2870 would therefore require a combined host-galaxy and intracluster-medium contribution of $\sim$150–200 pc cm^{-3} in the source frame, larger than the typical values assumed for field FRBs but well within the broad observed distribution of host DMs, particularly for sources embedded in dense environments. Alternatively, the burst could originate from a background source at $z \lesssim 0.2$ seen through the cluster field.

The candidate is presented as such, following the convention of X. Yang et al. (2021), who reserve the term detection for an $\mathrm{S/N} \geqslant 10$ and treat lower-significance events as candidate FRBs, because the evidence, although consistent with a dispersed astrophysical burst, is not yet sufficient to establish it: the significance is close to the search threshold and the burst's own S/N, at its matched width, is below it, the dispersed sweep cannot be seen directly in the dynamic spectrum at this S/N (Figure 1), and the implied rate is in tension with the known FRB population at the same fluence (Section 4.4). What supports it is the localization of the response in the DM–time plane, its persistence under progressively more aggressive channel masks (Table 2), its classification by FETCH, and its survival of visual inspection against the interference population of the site. Confirmation will require a repeat burst from the same position or an independent detection.

The results of this first campaign demonstrate that the IAR antennas, equipped with the ROACH backends, are capable of carrying out a blind FRB search and of producing candidates that can be followed up, and they support the continuation and extension of the monitoring program. The campaign will continue with extended observations of the Sculptor/Phoenix fields and, in particular, of the position of FRB 20251018, in order to search for possible repeat bursts from the same source. Monitoring of the A4013 and A2870 fields has in fact already continued through 2026 March (Table 1) without yielding a second firm detection: leaving aside the marginal candidates of Appendix A, we can put forward at most one candidate per supercluster field, and no repeat burst from the position of FRB 20251018 has been identified so far. We also plan to carry out simultaneous observations with both IAR antennas, A1 and A2: the detection of a burst in coincidence in two independent receivers separated by 120 m would provide a decisive discriminant against receiver-specific artifacts and against most local interference, although interference entering both antennas through their side lobes would survive this test and would have to be identified by its DM, and would allow us to confirm candidates near the detection threshold, such as those listed in Appendix A. A1 was not recording during the observation in which FRB 20251018 was detected, so no coincidence check is possible for this event.

The scientific return of the survey can be further enhanced by crossmatching our candidates with transients detected by other facilities. In particular, FRB candidates detected at the IAR can be searched for temporal and spatial coincidences with the gravitational-wave events reported by the LIGO-Virgo-KAGRA (LVK) Collaboration, along the lines of the joint CHIME/FRB-LVK analysis of R. Abbott et al. (2023); compact-binary mergers involving neutron stars are among the proposed FRB progenitor channels, and even null results provide useful constraints. Similarly, coincidences with electromagnetic counterparts at other wavelengths—most notably the high-energy bursts of magnetars, following the association of the Galactic FRB with SGR 1935+2154 (C. D. Bochenek et al. 2020; S. Mereghetti et al. 2020), but also with the broader population of X-ray, gamma-ray, and optical transients (B. Zhang 2024)—can help to establish the nature of the sources. The flexible, high-cadence scheduling of the IAR antennas makes them well suited both to systematic monitoring and to rapid follow-up of such multimessenger alerts in the southern sky.

Acknowledgments

C.O.L. gratefully acknowledges support from NSF awards AST-2319326, PHY-2207920, and PHY-2513442. We are very grateful to the staff of the IAR for their continuous technical support during the execution of this work. S.B.A.F. and E.Z. are PhD candidates with CONICET fellowships. G.E.R. and F.G. are CONICET researchers. G.E.R. and F.G. acknowledge financial support from the State Agency for Research of the Spanish Ministry of Science and Innovation under grant PID2022-136828NB-C41/AEI/10.13039/501100011033/, and from "ERDF A way of making Europe," European Union. G.E.R. also acknowledges support from PIP 0554 (CONICET). F.G. acknowledges support from PIBAA 1275 and PIP 0113 (CONICET). S.d.P. acknowledges support from ERC Advanced grant 789410.

Data Availability

The filterbank observations analyzed in this work, and the candidate cutouts of FRB 20251018 and of the marginal candidates listed in Appendix A, are available from the corresponding author upon reasonable request.

Facility: IAR.

Software: `PRESTO` (S. Ransom 2011), `FETCH` (D. Agarwal et al. 2020), `your` (K. Aggarwal et al. 2020), `Heimdall` (B. R. Barsdell et al. 2012; B. R. Barsdell & A. Jameson 2024), `FRB-faker` (L. J. M. Houben 2020; L. J. M. Houben et al. 2026), `RFIClean` (Y. Maan et al. 2021).

Appendix A
Marginal Potential Candidates

For the sake of completeness, in Table A1 we report the marginal FRB candidates found in this survey. Where the search recovered several closely spaced trials of the same event at neighboring DMs, only the trial with the highest `FETCH` score is listed. The final downselection was not based solely on the `FETCH` score: all triggers were also inspected visually, and candidates whose diagnostic plots suggested contamination by RFI were discarded, even when their `FETCH` scores were high. The purpose of the table is to allow these events to be recognized should an independent detection at another facility or wavelength coincide with one of them in time and position; none of them is claimed to be astrophysical, and the `FETCH` scores are classifier outputs, not calibrated probabilities (Section 2).

In the observations of the Sculptor Abell cluster A4013 (decl. $\delta = -35°16'00''$, R.A. $\alpha = 23^{h}31^{m}54^{s}$), we identified,

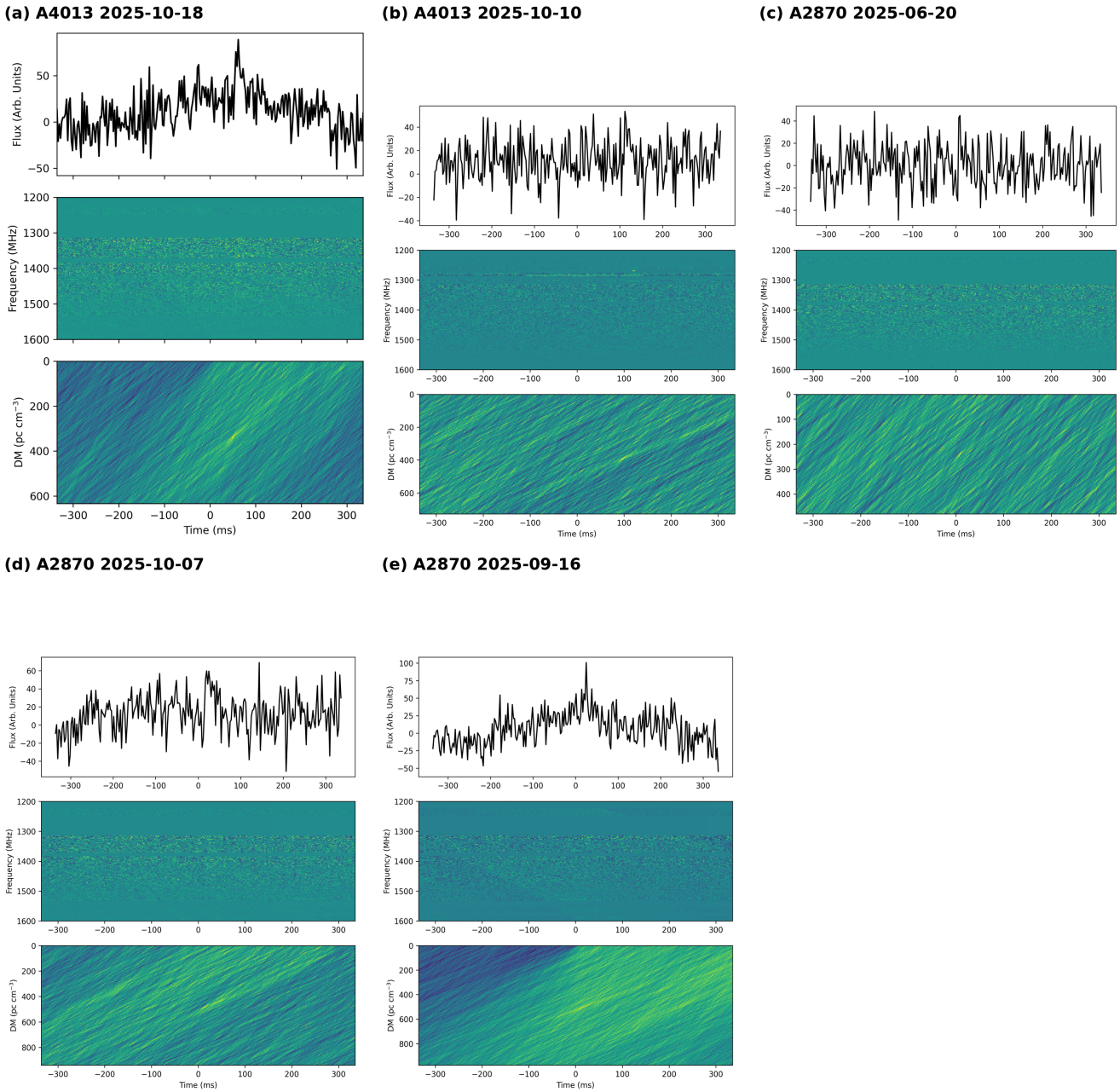

Figure A1. Search pipeline cutouts of the five marginal candidates of Table A1, in the same format as Figure 1 (671 ms window, 2.62 ms bins; top: dedispersed profile, middle: dedispersed dynamic spectrum, bottom: DM–time plane). (a) A4013 2025 October 18 (DM = 317, S/N = 8.41); (b) A4013 2025 October 10 (DM = 364, S/N = 9.23); (c) A2870 2025 June 20 (DM = 240, S/N = 12.47); (d) A2870 2025 October 7 (DM = 470, S/N = 8.40); (e) A2870 2025 September 16 (DM = 488, S/N = 8.90). The features that led to their classification as marginal are described in the text.

Table A1
Marginal FRB Candidates Identified in the Sculptor and Phoenix Region Observations

Field	Date	t_{start} (MJD)	t_{cand} (s)	DM (pc cm^{-3})	S/N	FETCH Score
A4013	2025-10-18	60966.115300925929	1073.0615600	317.00	8.41	0.9822453
A4013	2025-10-10	60958.148634259262	11,126.0998040	364.00	9.23	0.9970598
A2870	2025-10-07	60955.111828703702	1102.9774340	470.00	8.40	0.8548032
A2870	2025-09-16	60934.169467592590	1160.6419050	488.00	8.90	0.6974987
A2870	2025-06-20	60846.384050925924	17.0675400	240.00	12.47	0.5401518

Note. Dates are UTC dates of the start of the observation. Where several DM trials of the same event were recovered, only the trial with the highest FETCH score is listed.

in the observation of 2025 October 18 starting at MJD 60966.115300925929, a candidate at $t = 1073.0615600$ s, with a DM $= 317$ pc cm^{-3}, an S/N $= 8.41$, and a FETCH score of $p = 0.98$. Figure A1 shows the search pipeline cutouts of the five candidates, and the following features, noted on visual inspection, led us to classify each as marginal. For the A4013 event of 2025 October 18 (DM $= 317$), the profile shows a broad ($\sim$30 ms) excess rather than a sharp pulse, and the DM–time response is elongated along the dispersion diagonal instead of being concentrated at one DM. For the A4013 event of 2025 October 10 (DM $= 364$), the dynamic spectrum shows a bright narrowband feature at $\simeq$1285 MHz that brightens at the candidate time, and the profile is double peaked. For the A2870 event of 2025 June 20 (DM $= 240$), no pulse is visible in the 2.6 ms binned profile or in the DM–time plane despite the highest S/N in the table, which implies that the trigger was a single-sample (82 μs) spike, narrower than the $\simeq$0.6 ms of intra-channel dispersion smearing that any genuine burst at this DM must carry, and hence impulsive interference. For the A2870 event of 2025 October 7 (DM $= 470$), the profile shows a slow baseline drift across the window and no dominant peak, and the DM–time response is a broad band, as expected for a wide-boxcar trigger on baseline fluctuations. For the A2870 event of 2025 September 16 (DM $= 488$), a $\sim$200 ms excess in the profile and a DM–time response spread over several hundred parsecs per cubic centimeter indicate a broadband, long-duration feature rather than a millisecond burst. FRB 20251018, by contrast, shows a single dominant peak and a response in the DM–time plane that is compact and centered on the trial DM (Figure 1).

Appendix B
Details of the Validation Tests

In order to test our ability to identify FRBs in radio-astronomical data, we first performed a search on Parkes (Australia) data containing known FRB detections (E. F. Keane & E. Petroff 2015), available https://www.wis-tns.org/. This archival dataset comprises seven FRBs (FRB 010125, FRB 010621, FRB 010724, FRB 110220, FRB 110626, FRB 110703, and FRB 120127), with full-resolution SIGPROC filterbank files for all 13 beams of each pointing; the data for FRB 140514are available separately (E. Petroff 2014). In particular, we focused on the detection of FRB 110703, and we also injected a synthetic signal with `FRB-faker` (L. J. M. Houben 2020; L. J. M. Houben et al. 2026) that was successfully recovered by our pipeline. The filterbank data were processed and searched for bursts using the `Heimdall` single-pulse software package (B. R. Barsdell et al. 2012; B. R. Barsdell & A. Jameson 2024) and, independently, with `PRESTO` (S. Ransom 2011); the resulting candidates were then passed to FETCH (D. Agarwal et al. 2020) to assess whether they were genuine FRBs. We successfully recovered the FRBs with the correct arrival times and DMs. We also found in our limited study that `PRESTO` led to fewer false-positive detections than `Heimdall` for the IAR observations; hence, we adopted it by default in our searches.

As an additional blind test, in 2024 July–August one member of the team injected a synthetic single pulse with `FRB-faker` into the archival Parkes filterbank file containing FRB 110703 (observation of 2011 July 3; 1024 channels over 400 MHz at 1382 MHz, 64 μs sampling), without disclosing its parameters. The file was then independently analyzed by three members of our team with the pipeline described in Section 2, in this case with 64 sub-bands over $500 \leqslant$ DM $\leqslant 1525$ pc cm^{-3} (steps of 0.5 and 1.0 pc cm^{-3}, with downsampling factors of 8 and 12 below and above DM $= 1075$, respectively, following `DDplan.py`). All three recovered the same two events, and FETCH classified both with $p > 0.95$: the real FRB 110703, at $t = 118.61$ s, DM $= 1103$ pc cm^{-3} ($p = 0.95$), consistent with its cataloged DM $= 1103.6$ pc cm^{-3}; and the injected pulse, at $t = 35.00$ s and DM $= 1306$ pc cm^{-3} ($p = 0.99$). Remeasured on the dedispersed time series at 0.512 ms resolution, the injected pulse has a FWHM of 3.4 ms and a matched boxcar S/N of 14.5, and FRB 110703 a FWHM of 9.8 ms and a matched boxcar S/N of 11.1, the latter to be compared with the S/N $= 16$ and 4.3 ms width of the discovery (D. Thornton et al. 2013); a search of the same file dedispersed at other DMs confirmed that no other pulse was present.

Our next test made use of actual observations from the IAR. On 2024 September 23, we carried out five observations of 5 minutes (300 s) each, pointing antenna A2 at the zenith, and injected one synthetic FRB into each of the observations using `FRB-faker`. All injected bursts shared the same morphology —a pulse profile consisting of two subcomponents with widths (FWHM) of 2.8 and 4.0 ms, separated by $\sim$4 ms, each modeled as a Gaussian in the frequency domain (centered at 1463 and 1419 MHz with FWHMs of 180 and 250 MHz, respectively) with a spectral tilt of 8, which is the two-component model of a burst from FRB 121102 distributed with `FRB-faker` as its worked example—but each had a different DM, injection time, and S/N, as listed in Table B1. We were able to successfully recover all of these injected FRBs using the techniques described above. The recovered S/N is 0.4–0.8 of the nominal injected value (Table B1). The nominal value is defined by `FRB-faker` (L. J. M. Houben et al. 2026) as $A/(\sigma\sqrt{W})$, where A is the area of the noise-free, frequency-summed burst, W its full extent above zero ($\simeq$11 ms

Table B1
Synthetic FRBs Injected into Test Observations 1–5

Observation	DM (pc cm^{-3})	Time (s)	S/N	max_downfact	DM$_{rec}$ (pc cm^{-3})	S/N$_{rec}$
#1	560	160	28	45	528.1 (527.1)	10.4 (9.7)
#2	280	256	10	70	285.1	8.3
#3	410	86	45	70	408.1 (387.1)	29.2 (18.0)
#4	120	227	32	150	128.5	21.8
#5	356	136	17	70	337.1 (328.1)	9.5 (8.8)

Note. S/N is the nominal value set in `FRB-faker`. The test searches covered $100 \leqslant \mathrm{DM} \leqslant 1558.8$ pc cm^{-3} with the `max_downfact` listed. The last two columns give the trial DM and the `PRESTO` S/N (Section 2) of the highest-S/N trigger recovered for each injection; where the same burst produced a second, independent trigger at a neighboring trial DM, it is given in parentheses.

for this template at our resolution), and σ the rms of the frequency-summed, dedispersed noise of the target observation around the injection time, over all channels; for this template it is within 7% of the optimal-boxcar S/N, so it is essentially the S/N the burst would have if recovered at its exact DM in unmasked data, whereas the search reports the S/N of Section 2 at the trial DM of the recovered trigger, in the masked and detrended time series. Most of the deficit is accounted for by the DM offset of that trigger: the dispersive smearing $4.15\,\Delta\mathrm{DM}\,\Delta\nu^{-2}$ across the injected band, compared with the $\simeq$3.4 ms component width, predicts S/N factors of 0.37, 0.82, 0.96, 0.68 and 0.48 for injections #1–#5, against measured ratios of 0.37, 0.83, 0.65, 0.68 and 0.56, and the 16%–25% of the injected spectral weight that falls in masked channels contributes a further factor of $\simeq$0.9. This accounts for injections #1, #2, #4 and #5 to within the measurement scatter, but not for #3, whose measured ratio of 0.65 is well below the $\simeq$0.86 expected from these two effects; we have not identified the cause of the remaining deficit. Two injections were recovered close to the survey threshold, at S/N = 8.3 (#2) and 9.5 (#5), and a third at 10.4 (#1), so that the tests do probe the recovery of the pipeline at 8σ–10σ, the regime of FRB 20251018. The recovered DMs lie within -2 to $+8.5$ pc cm^{-3} of the injected values for injections #2, #3 and #4, but are offset by -32 and -19 pc cm^{-3} for #1 and #5, without an evident dependence on the injected or recovered S/N (#2, the faintest recovery at S/N = 8.3, is among the well-recovered ones). Evidently, for spectra confined to $\sim$200 MHz, and at an S/N of order 10, the DM of a single burst can be off by a few tens of parsecs per cubic centimeter, comparable to the ± 20 pc cm^{-3} adopted for FRB 20251018, whose live band is of similar width. For the system parameters adopted in Section 4.2, the 8σ detection threshold of our pipeline corresponds to a minimum detectable fluence of $\mathcal{F}_{\rm min} \approx 7\ (W\ \mathrm{ms}^{-1})^{1/2}$ Jy ms (equivalently, a minimum peak flux density of $\approx 7\ (W\ \mathrm{ms}^{-1})^{-1/2}$ Jy) for a burst of width W and the nominal 264 MHz of clean bandwidth, degrading to $\approx 9\ (W\ \mathrm{ms}^{-1})^{1/2}$ Jy ms for the 170 MHz retained by the most conservative mask of the channel-zapping test (Table 2). To these values must be added a $\sim$16% systematic uncertainty inherited from $T_{\rm sys}$. Together they define the fluence completeness of the survey.

ORCID iDs

Carlos O. Lousto https://orcid.org/0000-0002-6400-9640
Harsh Prajapati https://orcid.org/0009-0001-5703-0636
Ezequiel Zubieta https://orcid.org/0009-0009-5593-367X
Susana B. Araujo Furlan https://orcid.org/0000-0003-4027-4826
Guillermo Gancio https://orcid.org/0000-0003-1282-3031
Joaquín Pelle https://orcid.org/0000-0001-5820-8208
Gustavo E. Romero https://orcid.org/0000-0002-5260-1807
Federico García https://orcid.org/0000-0001-9072-4069
Santiago del Palacio https://orcid.org/0000-0002-5761-2417
Nathan Cahill https://orcid.org/0000-0002-6164-3291

References

Abbott, R., et al. 2023, ApJ, 955, 155
Abell, G. O., Corwin, H. G., Jr., & Olowin, R. P. 1989, ApJS, 70, 1
Agarwal, D., Aggarwal, K., Burke-Spolaor, S., Lorimer, D. R., & Garver-Daniels, N. 2020, MNRAS, 497, 1661
Aggarwal, K., et al. 2020, JOSS, 5, 2750
Amiri, M., Andersen, B. C., Bandura, K., et al. 2021, ApJS, 257, 59
Araujo Furlan, S. B., Romero, G. E., Zubieta, E., et al. 2026, A&A, 710, A13
Bannister, K. W., Shannon, R. M., Macquart, J.-P., et al. 2017, ApJL, 841, L12
Barsdell, B. R., Bailes, M., Barnes, D. G., et al. 2012, MNRAS, 422, 379
Barsdell, B. R., & Jameson, A. 2024, Heimdall: GPU accelerated transient detection pipeline for radio astronomy, Astrophysics Source Code Library,, ascl: 2407.016
Beniamini, P., Kumar, P., Ma, X., & Quataert, E. 2021, MNRAS, 502, 5134
Bhandari, S., Keane, E. F., Barr, E. D., et al. 2018, MNRAS, 475, 1427
Bochenek, C. D., Ravi, V., Belov, K. V., et al. 2020, Natur, 587, 59
Champion, D. J., Petroff, E., Kramer, M., et al. 2016, MNRAS, 460, L30
Chatterjee, S., Law, C. J., Wharton, R. S., et al. 2017, Natur, 541, 58
Chen, B. H., Hashimoto, T., Goto, T., et al. 2021, MNRAS, 509, 1227
CHIME/FRB Collaboration 2020, Natur, 582, 351
Connor, L., & van Leeuwen, J. 2018, AJ, 156, 256
Cordes, J. M., & Lazio, T. J. W. 2002, arXiv:astro-ph/0207156
Farah, W., Flynn, C., Bailes, M., et al. 2018, MNRAS, 478, 1209
Gajjar, V., Siemion, A. P. V., Price, D. C., et al. 2018, ApJ, 863, 2
Gancio, G., Lousto, C. O., Combi, L., et al. 2020, A&A, 633, A84
Giacintucci, S., Markevitch, M., Johnston-Hollitt, M., et al. 2020, ApJ, 891, 1
Hessels, J. W. T., Spitler, L. G., Seymour, A. D., et al. 2019, ApJL, 876, L23
Hickish, J., Dennett, F., Foster, G., et al. 2016, JAI, 5, 1641001
Houben, L. J. M. 2020, FRB Faker: Tool to inject SPs with complex morphologies in Filterbank data,, https://gitlab.com/houben.ljm/frb-faker
Houben, L. J. M., Falcke, H., Spitler, L. G., et al. 2026, A&A, 707, A10
Katz, J. I. 2016, MPLA, 31, 1630013
Keane, E. F., & Petroff, E. 2015, MNRAS, 447, 2852
Li, Z.-X., Gao, H., Ding, X.-H., Wang, G.-J., & Zhang, B. 2018, NatCo, 9, 3833
Lorimer, D. R., Bailes, M., McLaughlin, M. A., Narkevic, D. J., & Crawford, F. 2007, Sci, 318, 777
Lousto, C. O., Missel, R., Zubieta, E., et al. 2024, Rev. Mex. Astron. Astrofis. Ser. Conf., 56, 134
Lousto, C. O., Shrestha, R., Zubieta, E., et al. 2026, arXiv:2609.03056
Lu, W., Kumar, P., & Zhang, B. 2020, MNRAS, 498, 1397
Luo, J.-W., Zhu-Ge, J.-M., & Zhang, B. 2022, MNRAS, 518, 1629
Lyubarsky, Y. 2020, ApJ, 897, 1

Maan, Y., van Leeuwen, J., & Vohl, D. 2021, A&A, 650, A80
Macquart, J.-P., Prochaska, J. X., McQuinn, M., et al. 2020, Natur, 581, 391
McQuinn, M. 2013, ApJL, 780, L33
Mereghetti, S., Savchenko, V., Ferrigno, C., et al. 2020, ApJL, 898, L29
Metzger, B. D., Margalit, B., & Sironi, L. 2019, MNRAS, 485, 4091
Niu, C.-H., Li, D., Luo, R., et al. 2021, ApJL, 909, L8
Petroff, E. 2014, Fast Radio Burst Data: FRB 140514, Swinburne University of Technology, Research Data Australia, https://researchdata.edu.au/fast-radio-burst-frb-140514
Petroff, E., Hessels, J. W. T., & Lorimer, D. R. 2019, A&ARv, 27, 4
Petroff, E., Keane, E. F., Barr, E. D., et al. 2015, MNRAS, 451, 3933
Platts, E., Weltman, A., Walters, A., et al. 2019, PhR, 821, 1
Pleunis, Z., Good, D. C., Kaspi, V. M., et al. 2021b, ApJ, 923, 1
Pleunis, Z., Michilli, D., Bassa, C. G., et al. 2021a, ApJL, 911, L3
Prajapati, H., Araujo Furlan, S. B., Zubieta, E., et al. 2026, ATel, 17580, 1
Rafiei-Ravandi, M., Smith, K. M., Li, D., et al. 2021, ApJ, 922, 42
Ransom, S. 2011, PRESTO: PulsaR Exploration and Search TOolkit, Astrophysics Source Code Library, ascl: 1107.017
Ravi, V. 2019, NatAs, 3, 928
Raychaudhury, S. 1989, Natur, 342, 251
Scaramella, R., Baiesi-Pillastrini, G., Chincarini, G., Vettolani, G., & Zamorani, G. 1989, Natur, 338, 562
Shannon, R. M., Macquart, J.-P., Bannister, K. W., et al. 2018, Natur, 562, 386
Shirasaki, M., Takahashi, R., Osato, K., & Ioka, K. 2022, MNRAS, 512, 1730
Spitler, L. G., Scholz, P., Hessels, J. W. T., et al. 2016, Natur, 531, 202
Struble, M. F., & Rood, H. J. 1999, ApJS, 125, 35
Thornton, D., Stappers, B., Bailes, M., et al. 2013, Sci, 341, 53
Valotto, C. A., Muriel, H., Moore, B., & Lambas, D. G. 2004, ApJ, 603, 67
Wagstaff, K. L., Tang, B., Thompson, D. R., et al. 2016, PASP, 128, 084503
Walters, A., Weltman, A., Gaensler, B. M., Ma, Y.-Z., & Witzemann, A. 2018, ApJ, 856, 65
Werner, N., Zhuravleva, I., Canning, R. E. A., et al. 2016, MNRAS, 460, 2752
Xu, J., Feng, Y., Li, D., et al. 2023, Univ, 9, 330
Yamasaki, S., & Totani, T. 2020, ApJ, 888, 105
Yang, X., et al. 2021, MNRAS, 507, 3238
Yao, J. M., Manchester, R. N., & Wang, N. 2017, ApJ, 835, 29
Zhang, B. 2023, RvMP, 95, 035005
Zhang, B. 2024, ARNPS, 74, 89
Zhang, S.-B., Hobbs, G., Dai, S., et al. 2019, MNRAS, 484, L147
Zhang, Y. G., Gajjar, V., Foster, G., et al. 2018, ApJ, 866, 149
Zhou, D. J., Han, J. L., Zhang, B., et al. 2022, RAA, 22, 124001
Zhu-Ge, J.-M., Luo, J.-W., & Zhang, B. 2022, MNRAS, 519, 1823
Zubieta, E., García, F., del Palacio, S., et al. 2024, A&A, 689, A191
Zubieta, E., García, F., del Palacio, S., et al. 2025b, A&A, 694, A124
Zubieta, E., Missel, R., Araujo Furlan, S. B., et al. 2025a, A&A, 698, A72
Zubieta, E., Missel, R., Sosa Fiscella, V., et al. 2023, MNRAS, 521, 4504